A computational model for fluid leakage in heterogeneous layered porous media

Arzanfudi, MM; Al-Khoury, RIN; Sluys, LJ

DOI
10.1016/j.advwatres.2014.08.016

Publication date
2014

Document Version
Accepted author manuscript

Published in
Advances in Water Resources

A computational model for fluid leakage in heterogeneous layered porous media

Mehdi Musivand Arzanfudi [*] , Rafid Al-Khoury , Lambertus J. Sluys

Faculty of Civil Engineering and Geosciences, Delft University of Technology, P.O. Box 5048, 2600 GA Delft, The Netherlands

ABSTRACT

This paper introduces a new and computationally efficient model for the simulation of non-wetting phase leakage in a rigid heterogeneous layered medium domain constituting layers of different physical properties. Such a leakage exhibits a discontinuity in the saturation field at the interface between layers. The governing field equations are derived based on the averaging theory and solved numerically using a mixed finite element discretization scheme. This scheme entails solving different balance equations using different discretization techniques, which are tailored to accurately simulate the physical behavior of the primary state variables. A discontinuous non-wetting phase saturation – continuous water pressure formulation is adopted. The standard Galerkin finite element method is utilized to discretize the water phase pressure field, and the partition of unity finite element method is utilized to discretize the non-wetting phase saturation field. This mixed discretization scheme leads to a locally conservative system, giving accurate simulation of the saturation jump. The boundary between layers is embedded within the finite elements, alleviating the need to use the typical interface elements, and allowing for the use of structured, geometry-independent and relatively coarse meshes. The accuracy and capability of the proposed model are evaluated by verification and numerical examples covering water, DNAPL and CO_2 leakage through layers of different hydraulic properties.

Keywords: leakage; mixed discretization; partition of unity; heterogeneous layered porous media; CO2 sequestration

1 Introduction

Leakage of a non-wetting phase through a porous medium domain constituting heterogeneous layers can have a significant consequence on the environment and life on earth. Leakage of contaminants, infiltration of dense oil and Leakage of CO_2 to the ground surface or layers containing ground water, among many others, are currently considered one of the

[*] Correspondence to: Mehdi Musivand Arzanfudi

Faculty of Civil Engineering and Geosciences, Delft University of Technology, P.O. Box 5048, 2600 GA Delft, The Netherlands. Tel.: +31 (0)15 27 88216

E-mail: M.MusivandArzanfudi@tudelft.nl

main concerns of exploiting the earth space to cope with the current technological advancement.

Designing oil and gas fields, planning contaminant storages and selection of an appropriate geological formation for CO_2 sequestration require a good estimate of the amount of leakage that might take place in time. It is therefore vital to acquire computational tools capable of modelling this phenomenon. Modelling the leakage phenomenon accurately would not only give a good estimate of the amount of the leakage, but also an accurate approximation of the pore pressure distribution in the ground, and hence an accurate estimation of the mechanical behaviour of the region surrounding such projects.

Computational modelling of multiphase flow in geological formations often requires modelling heterogeneous porous medium domains of regional scales with irregular and complicated geometry. Discretization of such a geometry is rather demanding. It requires finite element meshes (finite difference or finite volume grids), which are relatively fine and aligned along the boundaries between the layers. As the layers usually differ in porosity, permeability, and capillary entry pressure, fields generated by the fluid flow exhibit a jump at the boundary between them. This effect, in many cases, cannot be captured by standard numerical discretization schemes.

The physics of fluid leakage at boundaries between layers with different hydraulic properties has been intensively studied by several researchers, including Van Duijn et al. [1], Helmig and Huber [2], Van Duijn et al. [3], and Fučík and Mikyška [4]. The capillary pressure plays an important role in the amount of leakage between two layers. Neighbouring layers in a heterogeneous layered medium have different capillary pressure-saturation relationships. Fig. 1 shows typical Brooks and Corey capillary pressure-saturation relationships [5] for two layers having different permeability.

To illustrate the effect of capillary pressure on fluid flow in heterogeneous layered domain, a layered porous medium occupied by a wetting phase (water) that is being displaced by a non-wetting phase (CO_2, for example) is considered. In such a medium, according to Brooks and Corey capillary pressure-saturation relationships, the following conditions exist at the boundary between two layers:

- The non-wetting phase does not leak from a layer of high permeability to a layer of low permeability unless the capillary pressure of the first layer exceeds a threshold pressure, known as the entry pressure (also called bubbling pressure), of the second layer. B^+ in Fig. 1 indicates the entry pressure of the high permeability layer, and B^- indicates that of the

low permeability layer. This condition gives rise to mass accumulation of the non-wetting phase at the boundary between the two layers.

- Accumulation of the non-wetting phase continues to occur for all capillary pressures between point B^+ and point A in Fig. 1. In this region the capillary pressure at the boundary between the two layers exhibits a discontinuity.
- Above point A, the non-wetting phase starts to infiltrate into the second layer. In this region, the capillary pressure is continuous, and as a result, the saturation field exhibits a discontinuity. The capillary pressure crossing points C and D, in Fig. 1 is an example of this condition. It can be seen that these two points correspond to water saturations S_w^+ and S_w^-, respectively.
- If the non-wetting phase flow occurs from the low permeability layer to the high permeability layer, the saturation field also exhibits a jump, but in this case in the form of suction. Initially, at $S_w = 1$, the entry pressure of the low permeability layer (B^-) is readily higher than that of the high permeability layer (B^+). Due to this, upon the arrival of the non-wetting phase to the boundary between the two layers, leakage (suction) immediately occurs, maintaining $S_w = 1$ in the low permeability layer and decreasing in the high permeability layer.

Note that the van Genuchten capillary pressure –saturation relationship [6] exhibits continuous capillary pressure at all times. However, as for Brooks and Corey, the van Genuchten relationship exhibits the saturation discontinuity at the boundary between layers. In this paper, we utilize the Brooks and Corey relationship, though extension to van Genuchten is straightforward.

The presence of these complicated physical conditions at the boundary between heterogeneous layers exerts sever difficulties on the numerical solution procedure. The standard Galerkin finite element method (SG), for instance, is not able to simulate this problem accurately, even if a fine mesh is utilized. Helmig and Huber (1998) intensively studied this problem and found that using SG to solve the infiltration of a Dense Non-Aqueous Phase Liquid (DNAPL) into a heterogeneous layered domain produces erroneous results. It fails to capture the discontinuity in the saturation field at the boundary between two layers, giving an incorrect impression of the amount of leakage.

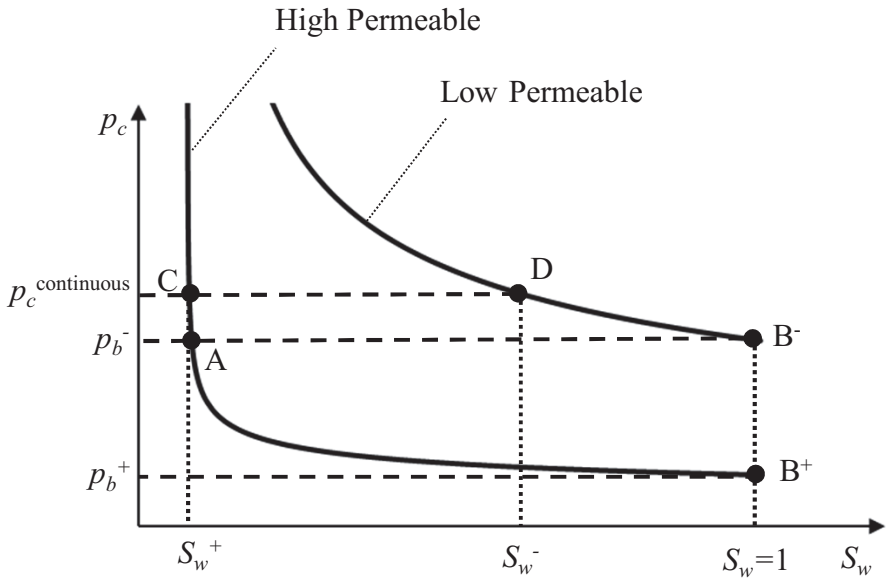

Fig. 1 Brooks and Corey capillary pressure-saturation relationships for two layers.

Therefore, in order to solve such a problem, the numerical scheme must be able to capture the discontinuity in the capillary pressure and saturation fields. In literature, several solution techniques with different discretization complexities have been proposed. Friis and Evje [7], Brenner et al. [8], Cances [9] and Szymkiewicz et al. [10] used the finite volume method for this purpose. Helmig and Huber [2] used the subdomain collocation finite volume method (Box Method) to solve the problem. This method comprises coupling between the finite element method and the finite volume method. Fučík and Mikyška [4] utilized a mixed hybrid finite element-discontinuous Galerkin discretization procedure (MHFE-DG).

Here, we solve this problem using a mixed finite element discretization scheme. This scheme differs from the well-known mixed FEM, such that in the mixed FEM, different state variables are utilized but a single discretization technique is adopted. However, in the mixed discretization scheme, we utilize different state variables and adopt different discretization techniques, depending on the nature of the state variable and the associated balance equations. We use the Partition of Unity finite element method (PUM) [11] to discretize the discontinuity in the non-wetting phase saturation field, and the standard Galerkin method (SG) to discretize the continuous water (wetting phase) pressure. We adopt the partition of unity property within the framework of the extended finite element method (XFEM), which entails decomposing the saturation field into a continuous part and a discontinuous part, where the latter is enhanced by use of a function which closely describes the nature of the jump in the field (the Heaviside function in case of strong discontinuity, for instance). The

main advantages of this method is two-folds. First, it captures the discontinuity accurately. Second, the discontinuity at the boundary between layers can be modelled regardless of the finite element mesh. Therefore, the mesh is not restricted to be aligned with the discontinuity, enabling the use of structured, geometry-independent and relatively coarse meshes.

This paper is organized as follows. In Section 2, governing equations based on a wetting pressure – non-wetting saturation formulation are derived. In Section 3, a detailed finite element formulation of the proposed PUM-SG model is given. In Section 4, a verification example and two numerical examples describing a DNAPL infiltration problem, and a 2D heterogeneous layered domain subjected to a CO_2 source are presented.

2 Governing Equations

The continuity equations of the wetting phase (formation water) and the non-wetting phase for isothermal, immiscible, incompressible two-phase flow in a rigid porous medium domain can be expressed as [12]

Water phase

$$\phi\frac{\partial S_w}{\partial t}+\frac{1}{\rho_w}\nabla\cdot\left[\rho_w\frac{\mathbf{k}k_{rw}}{\mu_w}\left(-\nabla p_w+\rho_w\mathbf{g}\right)\right]=Q_w \tag{1}$$

Non-wetting phase

$$\phi\frac{\partial S_n}{\partial t}+\frac{1}{\rho_n}\nabla\cdot\left[\rho_n\frac{\mathbf{k}k_{rn}}{\mu_n}\left(-\nabla p_n+\rho_n\mathbf{g}\right)\right]=Q_n \tag{2}$$

in which $\mathbf{g}$ is the gravity force vector, ρ_w is the water density, ρ_n is the non-wetting density, S_w is water saturation, S_n is non-wetting saturation, ϕ is the porosity, p_w and p_n are water and non-wetting pressure, $\mathbf{k}$ is the absolute permeability, k_{rw} and k_{rn} are water and non-wetting relative permeability (functions of saturation), μ_w and μ_n are water and non-wetting viscosity, and Q_w and Q_n are the volumetric source or sink terms. Note that subscript *n* is utilized to describe a non-wetting phase which can be oil, gas, or supercritical CO_2, among others.

We adopt a water phase pressure – non-wetting phase saturation formulation. In a porous domain, water and non-wetting phase are jointly occupying the pores, implying:

$$S_w+S_n=1 \tag{3}$$

and

$$p_c(S_n) = p_n - p_w \tag{4}$$

where $p_c(S_n)$ is the capillary pressure, a function of non-wetting phase saturation.

Applying the chain rule to Eq. (4), the non-wetting phase pressure gradient can be described as

$$\nabla p_n = \nabla p_w + \nabla p_c = \nabla p_w + \frac{dp_c}{dS_n}\nabla S_n \tag{5}$$

Substituting Eqs. (3) and (5) into Eqs. (1) and (2), in the absence of volumetric sources/sinks, the continuity balance equations can be described as

Water phase

$$-\phi\frac{\partial S_n}{\partial t} - \nabla\cdot\left[\mathbf{k}\lambda_w\left(\nabla p_w - \rho_w\mathbf{g}\right)\right] = 0 \tag{6}$$

Non-wetting phase

$$\phi\frac{\partial S_n}{\partial t} - \nabla\cdot\left[\mathbf{k}\lambda_n\left(\nabla p_w + \frac{dp_c}{dS_n}\nabla S_n - \rho_n\mathbf{g}\right)\right] = 0 \tag{7}$$

in which $\lambda_w = k_{rw}/\mu_w$ and $\lambda_n = k_{rn}/\mu_n$ are the water and non-wetting phase mobility. The advantage of this formulation is that the non-wetting phase saturation is made a primary variable, and hence can be explicitly discretized taking into account its discontinuity at the boundary between layers.

2.1 Constitutive relationships

In literature, there are several empirical formulations correlating the capillary pressure and relative permeability to saturation, such as van Genuchten [6] and Brooks and Corey [5]. Here, the Brooks and Corey formulation is adopted. Accordingly, the capillary pressure-saturation relationship is described as

$$p_c = p_b S_e^{-1/\hat{\theta}} \tag{8}$$

with

$$S_e = \frac{S_w - S_{rw}}{1 - S_{rw} - S_{rn}} \tag{9}$$

and the relative permeability-saturation relationships for the water and the non-wetting phases are described as

$$k_{rw} = S_e^{(2+3\hat{\theta})/\hat{\theta}} \tag{10}$$

$$k_{rn} = (1 - S_e)^2 \left(1 - S_e^{(2+\hat{\theta})/\hat{\theta}}\right) \tag{11}$$

where S_e is the effective saturation, S_{rw} is the irreducible water saturation, S_{rn} is the residual non-wetting phase saturation, $\hat{\theta}$ is the pore size distribution index and p_b is the entry pressure, corresponding to the capillary pressure needed to displace the water phase from the largest pore.

2.2 Initial and boundary conditions

Initially, the water pressure and the non-wetting phase saturation are set to

$$\begin{aligned} p_w &= p_{w0}(\mathbf{x}) \\ S_n &= S_{n0}(\mathbf{x}) \end{aligned} \quad \text{at } t = 0 \tag{12}$$

The Dirichlet boundary conditions are prescribed as

$$\begin{aligned} p_w &= \hat{p}_w \quad \text{on } \Gamma_w \\ S_n &= \hat{S}_n \quad \text{on } \Gamma_n \end{aligned} \tag{13}$$

in which $\Gamma = \Gamma_w \cup \Gamma_n$ is the Dirichlet boundary surface.

The relevant Neumann boundary conditions are:

Water flux

$$\mathbf{k}\lambda_w\rho_w\left(-\nabla p_w + \rho_w \mathbf{g}\right)\cdot\mathbf{n} = \hat{q}_w \text{ on } \Gamma_w^q \tag{14}$$

Non-wetting phase flux

$$\mathbf{k}\lambda_n\rho_n\left(-\nabla p_w - \nabla S_n \frac{dp_c}{dS_n} + \rho_n \mathbf{g}\right)\cdot\mathbf{n} = \hat{q}_n \text{ on } \Gamma_n^q \tag{15}$$

in which $\mathbf{n}$ is the outward normal to the boundary and $\Gamma^q = \Gamma_w^q \cup \Gamma_n^q$ is the Neumann boundary surface. The boundaries Γ and Γ^q are shown in Fig. 2.

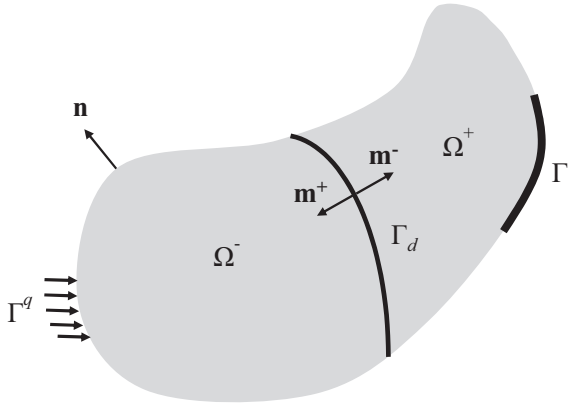

Fig. 2 Domain definition.

3 Mixed Finite Element Discretization

Eqs. (6)-(11), together with the initial and boundary conditions, Eqs. (12)-(15), represent an initial and boundary value problem of isothermal incompressible immiscible two-phase flow. This problem is solved here using a mixed finite element discretization scheme. This scheme entails solving different balance equations using different discretization schemes, which are tailored to accurately describe the nature of the primary state variables.

3.1 PUM-SG Formulation

Eqs. (6) and (7) are utilized here to describe multiphase flow in an initially saturated domain injected by a non-wetting phase. The water pressure is continuous even at the boundaries between layers, but the non-wetting phase saturation and capillary pressure (under certain conditions, described in the Introduction) exhibit a jump across the boundaries between layers. Considering this mixed nature of the involved variables, we utilize the standard Galerkin finite element method to discretize the water pressure field, and the partition of unity finite element method to discretize the saturation field. This kind of a mixed finite element discretization has been introduced by Al-Khoury and Sluys [13] to model fluid flow in fracturing porous media, and employed by [14, 15] to model coupled electrokinetic–hydromechanic processes in CO_2 geo-sequestration in single and double porosity porous medium domains. The difference, however, is that in this scheme a geometrical discontinuity is modelled, whereas in the previous ones either a discontinuity across a crack in the solid phase or a moving front of fluid phase were modelled.

Accordingly, using the Galerkin finite element method, the water pressure can be discretized as

$$p_w(\mathbf{x},t)=\sum_{i\in I} N_i(\mathbf{x})\, p_{wi}(t)=\mathbf{N}(\mathbf{x})\mathbf{p}_w(t) \tag{16}$$

in which I is the set of all nodes in the domain, $N_i(\mathbf{x})$ is the shape function of node i evaluated at $\mathbf{x}$, $p_{wi}(t)$ is the nodal value of water pressure for node i evaluated at time t, $\mathbf{N}(\mathbf{x})$ is the nodal vector of shape functions, and $\mathbf{p}_w(t)$ is the nodal vector of water pressure.

Using the partition of unity finite element method, the non-wetting phase saturation field can be discretized as

$$\begin{aligned} S_n(\mathbf{x},t)&=\sum_{i\in I} N_i(\mathbf{x})S_{ni}(t)+\sum_{i\in I^*} N_i^{eh}(\mathbf{x})\bar{S}_{ni}(t)\\ &=\mathbf{N}(\mathbf{x})\mathbf{S}_n(t)+\mathbf{N}^{eh}(\mathbf{x})\tilde{\mathbf{S}}_n(t)\end{aligned} \tag{17}$$

where I^* is the subset of enriched nodes, Fig. 3, $S_{ni}(t)$ and $\tilde{S}_{ni}(t)$ are the conventional and additional (extended) nodal values associated with the non-wetting phase saturation for node i, $N_i^{eh}(\mathbf{x})$ is an enriched shape function for node i, and $\mathbf{S}_n(t)$, $\tilde{\mathbf{S}}_n(t)$ and $\mathbf{N}^{eh}(\mathbf{x})$ are the associated nodal vectors. $\mathbf{N}^{eh}(\mathbf{x})$ is defined as

$$\mathbf{N}^{eh}(\mathbf{x})=\mathbf{N}(\mathbf{x})H(\mathbf{x}) \tag{18}$$

where $H(\mathbf{x})$ is any function that can closely describe the profile of the field within an element. Here, the Heaviside function is utilized, that reads

$$H(\mathbf{x})=\begin{cases}0 & \mathbf{x}\in\Omega^-\\ 1 & \mathbf{x}\in\Omega^+\end{cases} \tag{19}$$

in which Ω^+ and Ω^- represent subdomains occupied by two different layers, schematically illustrated in Fig. 2.

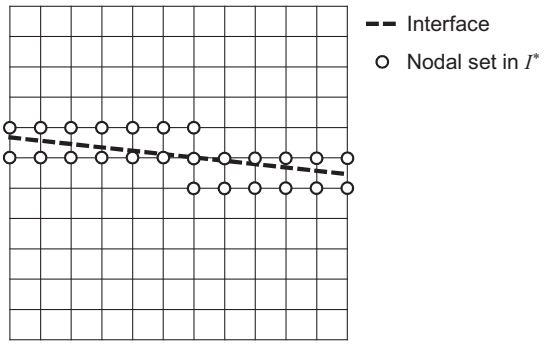

Fig. 3 Subset of enriched nodes.

The weak form of Eqs. (6) and (7) can be obtained using the weighted residual method. To compensate for the extra degrees of freedom introduced by PUM in Eq. (17), two different weight functions are necessary. A continuous weight function w is utilized for the water mass continuity equation, Eq. (6); and a discontinuous weight function w' is utilized for the non-wetting phase mass continuity equation, Eq. (7); giving

Water phase

$$\int_{\Omega} w\left\{-\phi\frac{\partial S_n}{\partial t}-\nabla\cdot\left[\mathbf{k}\lambda_w\left(\nabla p_w-\rho_w\mathbf{g}\right)\right]\right\}d\Omega=0 \tag{20}$$

Non-wetting phase

$$\int_{\Omega} w'\left\{\phi\frac{\partial S_n}{\partial t}-\nabla\cdot\left[\mathbf{k}\lambda_n\left(\nabla p_w+\frac{dp_c}{dS_n}\nabla S_n-\rho_n\mathbf{g}\right)\right]\right\}d\Omega=0 \tag{21}$$

where

$$w=\mathbf{N} \tag{22}$$

$$w'=\mathbf{N}+\mathbf{N}^{eh} \tag{23}$$

in which the dependencies on the spatial and temporal coordinates are discarded for simplicity of notation.

Substituting Eqs. (22) into Eqs. (20) and applying Green's theorem yields

$$\begin{aligned}&-\int_{\Omega}\mathbf{N}^T\phi\left(\mathbf{N}\dot{\mathbf{S}}_n+\mathbf{N}^{eh}\dot{\tilde{\mathbf{S}}}_n\right)d\Omega+\int_{\Omega}\nabla\mathbf{N}^T\mathbf{k}\lambda_w\nabla\mathbf{N}\mathbf{p}_w d\Omega\\&\quad-\int_{\Omega}\nabla\mathbf{N}^T\mathbf{k}\lambda_w\rho_w\mathbf{g}d\Omega+\frac{1}{\rho_w}\int_{\Gamma_w^q}\mathbf{N}^T\hat{q}_w d\Gamma=0\end{aligned} \tag{24}$$

Substituting Eq. (23) into Eq. (21) and applying Green's theorem yields two equations: one representing the continuous field and another the discontinuous field, as

$$\begin{aligned}&\int_{\Omega}\mathbf{N}^T\phi\left(\mathbf{N}\dot{\mathbf{S}}_n+\mathbf{N}^{eh}\dot{\tilde{\mathbf{S}}}_n\right)d\Omega+\int_{\Omega}\nabla\mathbf{N}^T\mathbf{k}\lambda_n\nabla\mathbf{N}\mathbf{p}_w d\Omega+\int_{\Omega}\nabla\mathbf{N}^T\mathbf{k}\lambda_n\frac{dp_c}{dS_n}\nabla\mathbf{N}\mathbf{S}_n\,d\Omega\\&\quad+\int_{\Omega^+}\nabla\mathbf{N}^T\mathbf{k}\lambda_n\frac{dp_c}{dS_n}\nabla\mathbf{N}^{eh}\tilde{\mathbf{S}}_n\,d\Omega-\int_{\Omega}\nabla\mathbf{N}^T\mathbf{k}\lambda_n\rho_n\mathbf{g}d\Omega+\frac{1}{\rho_n}\int_{\Gamma_n^q}\mathbf{N}^T\hat{q}_n d\Gamma=0\end{aligned} \tag{25}$$

$$\int_{\Omega^+}(\mathbf{N}^{eh})^T\phi(\mathbf{N}\dot{\mathbf{S}}_n+\mathbf{N}^{eh}\dot{\tilde{\mathbf{S}}}_n)d\Omega+\int_{\Omega^+}(\nabla\mathbf{N}^{eh})^T\mathbf{k}\lambda_n\nabla\mathbf{N}\mathbf{p}_w d\Omega$$
$$+\int_{\Omega^+}(\nabla\mathbf{N}^{eh})^T\mathbf{k}\lambda_n\frac{dp_c}{dS_n}(\nabla\mathbf{N}\mathbf{S}_n+\nabla\mathbf{N}^{eh}\tilde{\mathbf{S}}_n)d\Omega \tag{26}$$
$$-\int_{\Omega^+}(\nabla\mathbf{N}^{eh})^T\mathbf{k}\lambda_n\rho_n\mathbf{g}d\Omega+\frac{1}{\rho_n}\int_{\Gamma_n^{q+}}(\mathbf{N}^{eh})^T\hat{q}_n d\Gamma-\frac{1}{\rho_n}\int_{\Gamma_d}(\mathbf{N}^{eh})^T q_n^{\Gamma d}\,d\Gamma=0$$

where Γ_d is the boundary between layers as shown in Fig. 2, Γ_n^{q+} is the part of Γ_n^q which acts on the boundary of Ω^+, and $q_n^{\Gamma d}$ is the non-wetting phase flow rate across the boundary between layers, describing the leakage between layers; defined as

$$q_n^{\Gamma d}=\mathbf{q}_n^{\Gamma d}\cdot\mathbf{m} \tag{27}$$

where $\mathbf{q}_n^{\Gamma d}$ is the associated flux vector, and **m** is the unit normal vector to the interface. This leakage term is treated in details in Section 3.3.

3.2 Linearization

The resulting weak formulations, Eqs. (24)-(26), represent a set of semi-discrete nonlinear equations, where the nonlinearity arises from the constitutive relationships between the relative permeability and water saturation, and between the capillary pressure and water saturation, described in Eqs. (8)-(11). A fully implicit approach is adopted to solve the resulting nonlinear system of equations. Since the nonlinearity is due to scalar coefficients (i.e. λ_w, λ_n, dp_c/dS_n, etc.), and as the constitutive relationships are continuous, it is convenient to linearize these equations using Taylor series expansions up to the first order (equivalent to the standard Newton-Raphson). The Taylor series expansion of a function $g(x)$ around a point $\bar{x}$ is given by

$$g(x)=g(\bar{x})+\left.\frac{dg}{dx}\right|_{x=\bar{x}}(x-\bar{x})+\text{higher order terms} \tag{28}$$

For example, the mobility parameter λ_w at the current iteration $r+1$, can be linearized as

$$\lambda_w^{r+1}=\lambda_w(S_n^r)+\frac{d\lambda_w(S_n^r)}{dS_n}\delta S_n \tag{29}$$

with

$$\delta S_n=S_n^{r+1}-S_n^r \tag{30}$$

where the superscript r denotes the iteration number and the prefix δ denotes the increment of the state vector. Other nonlinear parameters can be linearized in the same manner.
The primary variables and their time derivatives can be written as

$$\begin{aligned} \mathbf{p}_w^{r+1} &= \mathbf{p}_w^r + \delta\mathbf{p}_w \qquad \mathbf{S}_n^{r+1} = \mathbf{S}_n^r + \delta\mathbf{S}_n \qquad \tilde{\mathbf{S}}_n^{r+1} = \tilde{\mathbf{S}}_n^r + \delta\tilde{\mathbf{S}}_n \\ \dot{\mathbf{p}}_w^{r+1} &= \dot{\mathbf{p}}_w^r + \delta\dot{\mathbf{p}}_w \qquad \dot{\mathbf{S}}_n^{r+1} = \dot{\mathbf{S}}_n^r + \delta\dot{\mathbf{S}}_n \qquad \dot{\tilde{\mathbf{S}}}_n^{r+1} = \dot{\tilde{\mathbf{S}}}_n^r + \delta\dot{\tilde{\mathbf{S}}}_n \end{aligned} \tag{31}$$

Using Brooks and Corey model given in Eqs. (8)-(11), and assuming a constant viscosity, the mobility gradients can be calculated analytically according to

$$\frac{d\lambda_w}{dS_n} = \frac{1}{\mu_w}\frac{dk_{rw}}{dS_e}\frac{dS_e}{dS_n} \tag{32}$$

$$\frac{d\lambda_n}{dS_n} = \frac{1}{\mu_n}\frac{dk_{rn}}{dS_e}\frac{dS_e}{dS_n} \tag{33}$$

$$\frac{d\eta_n}{dS_n} = \frac{d\lambda_n}{dS_n}\frac{dp_c}{dS_n} + \lambda_n\frac{d^2p_c}{{dS_n}^2} \tag{34}$$

where $\eta_n = \lambda_n\dfrac{dp_c}{dS_n}$.

It is worth mentioning that when the wetting phase vanishes, the term dp_c / dS_n, goes to infinity. To avoid this situation, we follow a regularization technique proposed in [16]. In this technique, the marginal values of capillary pressure are regularized. This means, instead of following Brooks-Corey relationships for very low wetting phase values, a linear approximation is used. However, more advanced regularization techniques can be found in [17-19].
Inserting Eqs. (29) and (31) into Eqs. (24)-(26), after rearrangements, gives

Water continuity equation: continuous field

$$\begin{aligned} &-\int_\Omega \mathbf{N}^T\phi\mathbf{N}\dot{\mathbf{S}}_n^r d\Omega - \int_\Omega \mathbf{N}^T\phi\mathbf{N}\delta\dot{\mathbf{S}}_n d\Omega - \int_\Omega \mathbf{N}^T\phi\mathbf{N}^{eh}\dot{\tilde{\mathbf{S}}}_n^r d\Omega - \int_\Omega \mathbf{N}^T\phi\mathbf{N}^{eh}\delta\dot{\tilde{\mathbf{S}}}_n d\Omega \\ &\quad + \int_\Omega \nabla\mathbf{N}^T\mathbf{k}\lambda_w^r\nabla\mathbf{N}\mathbf{p}_w^r d\Omega + \int_\Omega \nabla\mathbf{N}^T\mathbf{k}\lambda_w^r\nabla\mathbf{N}\delta\mathbf{p}_w d\Omega \\ &\quad + \int_\Omega \nabla\mathbf{N}^T\mathbf{k}\nabla\mathbf{N}\mathbf{p}_w^r\left(\frac{d\lambda_w}{dS_n}\mathbf{N}\delta\mathbf{S}_n\right)d\Omega + \int_\Omega \nabla\mathbf{N}^T\mathbf{k}\nabla\mathbf{N}\mathbf{p}_w^r\left(\frac{d\lambda_w}{dS_n}\mathbf{N}^{eh}\delta\tilde{\mathbf{S}}_n\right)d\Omega \\ &\quad - \int_\Omega \nabla\mathbf{N}^T\mathbf{k}\lambda_w^r\rho_w\mathbf{g}d\Omega - \int_\Omega \nabla\mathbf{N}^T\mathbf{k}\rho_w\mathbf{g}\left(\frac{d\lambda_w}{dS_n}\mathbf{N}\delta\mathbf{S}_n\right)d\Omega \\ &\quad - \int_\Omega \nabla\mathbf{N}^T\mathbf{k}\rho_w\mathbf{g}\left(\frac{d\lambda_w}{dS_n}\mathbf{N}^{eh}\delta\tilde{\mathbf{S}}_n\right)d\Omega + \frac{1}{\rho_w}\int_{\Gamma_w^q}\mathbf{N}^T\hat{q}_w d\Gamma = 0 \end{aligned} \tag{35}$$

Non-wetting phase continuity equation: continuous field

$$\int_\Omega \mathbf{N}^T \phi \mathbf{N} \dot{\mathbf{S}}_n^r d\Omega + \int_\Omega \mathbf{N}^T \phi \mathbf{N} \delta \dot{\mathbf{S}}_n d\Omega + \int_\Omega \mathbf{N}^T \phi \mathbf{N}^{eh} \dot{\tilde{\mathbf{S}}}_n^r d\Omega + \int_\Omega \mathbf{N}^T \phi \mathbf{N}^{eh} \delta \dot{\tilde{\mathbf{S}}}_n d\Omega$$
$$+ \int_\Omega \nabla \mathbf{N}^T \mathbf{k} \lambda_n^r \nabla \mathbf{N} \mathbf{p}_w^r d\Omega + \int_\Omega \nabla \mathbf{N}^T \mathbf{k} \lambda_n^r \nabla \mathbf{N} \delta \mathbf{p}_w d\Omega + \int_\Omega \nabla \mathbf{N}^T \mathbf{k} \nabla \mathbf{N} \mathbf{p}_w^r \left(\frac{d\lambda_n}{dS_n} \mathbf{N} \delta \mathbf{S}_n \right) d\Omega$$
$$+ \int_\Omega \nabla \mathbf{N}^T \mathbf{k} \nabla \mathbf{N} \mathbf{p}_w^r \left(\frac{d\lambda_n}{dS_n} \mathbf{N}^{eh} \delta \tilde{\mathbf{S}}_n \right) d\Omega + \int_\Omega \nabla \mathbf{N}^T \mathbf{k} \eta_n^r \nabla \mathbf{N} \mathbf{S}_n^r \, d\Omega + \int_\Omega \nabla \mathbf{N}^T \mathbf{k} \eta_n^r \nabla \mathbf{N} \delta \mathbf{S}_n \, d\Omega$$
$$+ \int_\Omega \nabla \mathbf{N}^T \mathbf{k} \nabla \mathbf{N} \mathbf{S}_n^r \left(\frac{d\eta_n}{dS_n} \mathbf{N} \delta \mathbf{S}_n \right) d\Omega + \int_\Omega \nabla \mathbf{N}^T \mathbf{k} \nabla \mathbf{N} \mathbf{S}_n^r \left(\frac{d\eta_n}{dS_n} \mathbf{N}^{eh} \delta \tilde{\mathbf{S}}_n \right) d\Omega$$
$$+ \int_{\Omega^+} \nabla \mathbf{N}^T \mathbf{k} \eta_n^r \nabla \mathbf{N}^{eh} \tilde{\mathbf{S}}_n^r \, d\Omega + \int_{\Omega^+} \nabla \mathbf{N}^T \mathbf{k} \eta_n^r \nabla \mathbf{N}^{eh} \delta \tilde{\mathbf{S}}_n \, d\Omega + \int_\Omega \nabla \mathbf{N}^T \mathbf{k} \nabla \mathbf{N}^{eh} \tilde{\mathbf{S}}_n^r \left(\frac{d\eta_n}{dS_n} \mathbf{N} \delta \mathbf{S}_n \right) d\Omega$$
$$+ \int_\Omega \nabla \mathbf{N}^T \mathbf{k} \nabla \mathbf{N}^{eh} \tilde{\mathbf{S}}_n^r \left(\frac{d\eta_n}{dS_n} \mathbf{N}^{eh} \delta \tilde{\mathbf{S}}_n \right) d\Omega - \int_\Omega \nabla \mathbf{N}^T \mathbf{k} \lambda_n^r \rho_n \mathbf{g} d\Omega - \int_\Omega \nabla \mathbf{N}^T \mathbf{k} \rho_n \mathbf{g} \left(\frac{d\lambda_n}{dS_n} \mathbf{N} \delta \mathbf{S}_n \right) d\Omega$$
$$- \int_\Omega \nabla \mathbf{N}^T \mathbf{k} \rho_n \mathbf{g} \left(\frac{d\lambda_n}{dS_n} \mathbf{N}^{eh} \delta \tilde{\mathbf{S}}_n \right) d\Omega + \frac{1}{\rho_n} \int_{\Gamma_n^q} \mathbf{N}^T \hat{q}_n d\Gamma = 0 \tag{36}$$

Non-wetting phase continuity equation: discontinuous field

$$\int_{\Omega^+} (\mathbf{N}^{eh})^T \phi \mathbf{N} \dot{\mathbf{S}}_n^r d\Omega + \int_{\Omega^+} (\mathbf{N}^{eh})^T \phi \mathbf{N} \delta \dot{\mathbf{S}}_n d\Omega + \int_{\Omega^+} (\mathbf{N}^{eh})^T \phi \mathbf{N}^{eh} \dot{\tilde{\mathbf{S}}}_n^r d\Omega$$
$$+ \int_{\Omega^+} (\mathbf{N}^{eh})^T \phi \mathbf{N}^{eh} \delta \dot{\tilde{\mathbf{S}}}_n d\Omega + \int_{\Omega^+} (\nabla \mathbf{N}^{eh})^T \mathbf{k} \lambda_n^r \nabla \mathbf{N} \mathbf{p}_w^r d\Omega + \int_{\Omega^+} (\nabla \mathbf{N}^{eh})^T \mathbf{k} \lambda_n^r \nabla \mathbf{N} \delta \mathbf{p}_w d\Omega$$
$$+ \int_{\Omega^+} (\nabla \mathbf{N}^{eh})^T \mathbf{k} \nabla \mathbf{N} \mathbf{p}_w^r \left(\frac{d\lambda_n}{dS_n} \mathbf{N} \delta \mathbf{S}_n \right) d\Omega + \int_{\Omega^+} (\nabla \mathbf{N}^{eh})^T \mathbf{k} \nabla \mathbf{N} \mathbf{p}_w^r \left(\frac{d\lambda_n}{dS_n} \mathbf{N}^{eh} \delta \tilde{\mathbf{S}}_n \right) d\Omega$$
$$+ \int_{\Omega^+} (\nabla \mathbf{N}^{eh})^T \mathbf{k} \eta_n^r \nabla \mathbf{N} \mathbf{S}_n^r \, d\Omega + \int_{\Omega^+} (\nabla \mathbf{N}^{eh})^T \mathbf{k} \eta_n^r \nabla \mathbf{N} \delta \mathbf{S}_n \, d\Omega$$
$$+ \int_{\Omega^+} (\nabla \mathbf{N}^{eh})^T \mathbf{k} \nabla \mathbf{N} \mathbf{S}_n^r \left(\frac{d\eta_n}{dS_n} \mathbf{N} \delta \mathbf{S}_n \right) d\Omega + \int_{\Omega^+} (\nabla \mathbf{N}^{eh})^T \mathbf{k} \nabla \mathbf{N} \mathbf{S}_n^r \left(\frac{d\eta_n}{dS_n} \mathbf{N}^{eh} \delta \tilde{\mathbf{S}}_n \right) d\Omega$$
$$+ \int_{\Omega^+} (\nabla \mathbf{N}^{eh})^T \mathbf{k} \eta_n^r \nabla \mathbf{N}^{eh} \tilde{\mathbf{S}}_n^r \, d\Omega + \int_{\Omega^+} (\nabla \mathbf{N}^{eh})^T \mathbf{k} \eta_n^r \nabla \mathbf{N}^{eh} \delta \tilde{\mathbf{S}}_n \, d\Omega$$
$$+ \int_{\Omega^+} (\nabla \mathbf{N}^{eh})^T \mathbf{k} \nabla \mathbf{N}^{eh} \tilde{\mathbf{S}}_n^r \left(\frac{d\eta_n}{dS_n} \mathbf{N} \delta \mathbf{S}_n \right) d\Omega + \int_{\Omega^+} (\nabla \mathbf{N}^{eh})^T \mathbf{k} \nabla \mathbf{N}^{eh} \tilde{\mathbf{S}}_n^r \left(\frac{d\eta_n}{dS_n} \mathbf{N}^{eh} \delta \tilde{\mathbf{S}}_n \right) d\Omega$$
$$- \int_{\Omega^+} (\nabla \mathbf{N}^{eh})^T \mathbf{k} \lambda_n^r \rho_n \mathbf{g} d\Omega - \int_{\Omega^+} (\nabla \mathbf{N}^{eh})^T \mathbf{k} \rho_n \mathbf{g} \left(\frac{d\lambda_n}{dS_n} \mathbf{N} \delta \mathbf{S}_n \right) d\Omega$$
$$- \int_{\Omega^+} (\nabla \mathbf{N}^{eh})^T \mathbf{k} \rho_n \mathbf{g} \left(\frac{d\lambda_n}{dS_n} \mathbf{N}^{eh} \delta \tilde{\mathbf{S}}_n \right) d\Omega + \frac{1}{\rho_n} \int_{\Gamma_n^{q+}} (\mathbf{N}^{eh})^T \hat{q}_n d\Gamma - \frac{1}{\rho_n} \int_{\Gamma_d} (\mathbf{N}^{eh})^T q_n^{\Gamma d} \, d\Gamma = 0 \tag{37}$$

In a concise form, Eq. (35) can be written as

$$\mathbf{K}_{11}\delta\mathbf{p}_w+\mathbf{K}_{12}\delta\mathbf{S}_n+\mathbf{K}_{13}\delta\tilde{\mathbf{S}}_n+\mathbf{C}_{12}\delta\dot{\mathbf{S}}_n+\mathbf{C}_{13}\delta\dot{\tilde{\mathbf{S}}}_n=\mathbf{f}_1-(\mathbf{K}_{11}^0\mathbf{p}_w^r+\mathbf{C}_{12}^0\dot{\mathbf{S}}_n^r+\mathbf{C}_{13}^0\dot{\tilde{\mathbf{S}}}_n^r) \tag{38}$$

Similarly, Eqs. (36) and (37) can be written as

$$\begin{aligned}\mathbf{K}_{21}\delta\mathbf{p}_w+\mathbf{K}_{22}\delta\mathbf{S}_n+\mathbf{K}_{23}\delta\tilde{\mathbf{S}}_n+\mathbf{C}_{22}\delta\dot{\mathbf{S}}_n+\mathbf{C}_{23}\delta\dot{\tilde{\mathbf{S}}}_n\\ =\mathbf{f}_2-(\mathbf{K}_{21}^0\mathbf{p}_w^r+\mathbf{K}_{22}^0\mathbf{S}_n^r+\mathbf{K}_{23}^0\tilde{\mathbf{S}}_n^r+\mathbf{C}_{22}^0\dot{\mathbf{S}}_n^r+\mathbf{C}_{23}^0\dot{\tilde{\mathbf{S}}}_n^r)\end{aligned} \tag{39}$$

$$\begin{aligned}\mathbf{K}_{31}\delta\mathbf{p}_w+\mathbf{K}_{32}\delta\mathbf{S}_n+\mathbf{K}_{33}\delta\tilde{\mathbf{S}}_n+\mathbf{C}_{32}\delta\dot{\mathbf{S}}_n+\mathbf{C}_{33}\delta\dot{\tilde{\mathbf{S}}}_n\\ =\mathbf{f}_3-(\mathbf{K}_{31}^0\mathbf{p}_w^r+\mathbf{K}_{32}^0\mathbf{S}_n^r+\mathbf{K}_{33}^0\tilde{\mathbf{S}}_n^r+\mathbf{C}_{32}^0\dot{\mathbf{S}}_n^r+\mathbf{C}_{33}^0\dot{\tilde{\mathbf{S}}}_n^r)\end{aligned} \tag{40}$$

Collecting Eqs. (38)-(40) in a matrix form, yields

$$\begin{aligned}&\begin{pmatrix}\mathbf{K}_{11}&\mathbf{K}_{12}&\mathbf{K}_{13}\\ \mathbf{K}_{21}&\mathbf{K}_{22}&\mathbf{K}_{23}\\ \mathbf{K}_{31}&\mathbf{K}_{32}&\mathbf{K}_{33}\end{pmatrix}\begin{Bmatrix}\delta\mathbf{p}_w\\ \delta\mathbf{S}_n\\ \delta\tilde{\mathbf{S}}_n\end{Bmatrix}+\begin{pmatrix}0&\mathbf{C}_{12}&\mathbf{C}_{13}\\ 0&\mathbf{C}_{22}&\mathbf{C}_{23}\\ 0&\mathbf{C}_{32}&\mathbf{C}_{32}\end{pmatrix}\begin{Bmatrix}\delta\dot{\mathbf{p}}_w\\ \delta\dot{\mathbf{S}}_n\\ \delta\dot{\tilde{\mathbf{S}}}_n\end{Bmatrix}\\ &=\begin{Bmatrix}\mathbf{f}_1\\ \mathbf{f}_2\\ \mathbf{f}_3\end{Bmatrix}-\begin{pmatrix}\mathbf{K}_{11}^0&0&0\\ \mathbf{K}_{21}^0&\mathbf{K}_{22}^0&\mathbf{K}_{23}^0\\ \mathbf{K}_{31}^0&\mathbf{K}_{32}^0&\mathbf{K}_{33}^0\end{pmatrix}\begin{Bmatrix}\mathbf{p}_w^r\\ \mathbf{S}_n^r\\ \tilde{\mathbf{S}}_n^r\end{Bmatrix}-\begin{pmatrix}0&\mathbf{C}_{12}^0&\mathbf{C}_{13}^0\\ 0&\mathbf{C}_{22}^0&\mathbf{C}_{23}^0\\ 0&\mathbf{C}_{32}^0&\mathbf{C}_{33}^0\end{pmatrix}\begin{Bmatrix}\dot{\mathbf{p}}_w^r\\ \dot{\mathbf{S}}_n^r\\ \dot{\tilde{\mathbf{S}}}_n^r\end{Bmatrix}\end{aligned} \tag{41}$$

The matrix entries of this equation are given in Appendix A.

Eq. (41) contains an extra degree of freedom as compared to that if the standard Galerkin method is utilized to discretize all variables. This entails that the system of equations that needs to be solved is larger. However, this increase is minor, as the extra degree of freedom is only added to the nodes where the element intersects the boundary between layers. This increase in the system size is compensated by the advantages of the partition of unity method. This method is effectively mesh-independent, allowing thus for the utilization of relatively coarse meshes. Also, as the boundary between the layers is described within the element, the mesh can be independent of the alignment of the involved layers, allowing thus the use of structured meshes.

Time discretization of the semi-discrete equation, Eq. (41), can be done using a standard time discretization algorithm. Here, the theta-method [12] is utilized. A direct sparse linear solver is utilized to solve the linearized algebraic set of equations.

3.3 Leakage term

The leakage term $q_n^{\Gamma d}$ in Eq. (26) is the mass flux, which describes the rate of mass flow per unit area of the interface between two layers. At the interface between two layers, the following conditions exist [1, 2, 4] (see Fig. 1):

1. Immobile non-wetting phase:

$$\begin{aligned} &q_n^{\Gamma d} = 0 \\ &p_c^+ \neq p_c^- \end{aligned} \tag{42}$$

2. Mobile non-wetting phase:

$$\begin{aligned} &q_n^{\Gamma d} > 0 \\ &p_c^+ = p_c^- \end{aligned} \tag{43}$$

in which the superscripts ($^+$) and ($^-$) indicate the field values at the Ω^+ side and the Ω^- side of the interface, respectively (see Fig. 2).

Substituting Eqs. (3), (8), and (10) into the second equation of Eq. (43) leads to

$$p_b^+ \left(\frac{1-\left(S_n^{i+1}\right)^+ - S_{rw}^+}{1-S_{rw}^+ - S_{rn}^+} \right)^{-1/\hat{\theta}^+} = p_b^- \left(\frac{1-\left(S_n^{i+1}\right)^- - S_{rw}^-}{1-S_{rw}^- - S_{rn}^-} \right)^{-1/\hat{\theta}^-} \tag{44}$$

where $\left(S_n^{i+1}\right)^+$ and $\left(S_n^{i+1}\right)^-$ are the non-wetting phase saturations corresponding to the current time step i+1, that can be delineated as

$$\left(S_n^{i+1}\right)^+ = \left(S_n^i\right)^+ + \Delta S_n^+ \tag{45}$$

$$\left(S_n^{i+1}\right)^- = \left(S_n^i\right)^- + \Delta S_n^- \tag{46}$$

in which ΔS_n^+ and ΔS_n^- are the current saturation changes that are necessary to satisfy the capillary pressure field condition given in the second equation of Eq. (43).

Substituting Eqs. (45) and (46) into Eq. (44) gives

$$p_b^+ \left(\frac{1-\left(S_n^i\right)^+ - \Delta S_n^+ - S_{rw}^+}{1-S_{rw}^+ - S_{rn}^+} \right)^{-1/\hat{\theta}^+} - p_b^- \left(\frac{1-\left(S_n^i\right)^- - \Delta S_n^- - S_{rw}^-}{1-S_{rw}^- - S_{rn}^-} \right)^{-1/\hat{\theta}^-} = 0 \tag{47}$$

where all parameters are known, except ΔS_n^+ and ΔS_n^-. Since Eq. (47) contains two unknowns, another equation is necessary.

Following the conservation of mass, the mass entering the interface should be equal to the mass leaving, implying that the mass flow rate of the non-wetting phase is equal at both sides of the interface, as

$$\mathbf{q}_n^{\Gamma d+} \cdot \mathbf{m}^+ = \mathbf{q}_n^{\Gamma d-} \cdot \mathbf{m}^- \tag{48}$$

where $\mathbf{m}^+$ is the unit vector pointing out of Ω^+ zone into Ω^- zone, and $\mathbf{m}^-$ is the unit vector pointing out of Ω^- zone into Ω^+ zone, with

$$\mathbf{m}^+ = -\mathbf{m}^- \tag{49}$$

giving

$$q_n^{\Gamma d+} = -q_n^{\Gamma d-} \tag{50}$$

where these mass fluxes can be described as

$$q_n^{\Gamma d+} = -\frac{\phi^+ \Delta S_n^+ \rho_n V^+}{A \Delta t} \tag{51}$$

$$q_n^{\Gamma d-} = -\frac{\phi^- \Delta S_n^- \rho_n V^-}{A \Delta t} \tag{52}$$

in which A is the interface surface area and V^+ and V^- are the volumes of the non-wetting phase mass accumulating just before and after the interface, respectively. Assuming $V^+ = V^-$ and substituting Eqs. (51) and (52) into Eq. (50) gives

$$\Delta S_n^- = -\frac{\phi^+}{\phi^-} \Delta S_n^+ \tag{53}$$

Substituting Eq. (53) into Eq. (47) would eliminate ΔS_n^-, giving an algebraic equation with one unknown (ΔS_n^+), as

$$p_b^+ \left(\frac{1 - \left(S_n^i\right)^+ - \Delta S_n^+ - S_{rw}^+}{1 - S_{rw}^+ - S_{rn}^+} \right)^{-1/\hat{\theta}^+} - p_b^- \left(\frac{1 - \left(S_n^i\right)^- + \frac{\phi^+}{\phi^-} \Delta S_n^+ - S_{rw}^-}{1 - S_{rw}^- - S_{rn}^-} \right)^{-1/\hat{\theta}^-} = 0 \tag{54}$$

Having ΔS_n^+, the mass flux across the boundary between two layers can then be calculated using Eq. (51). This equation can be written as

$$q_n^{\Gamma d+} = -\frac{\phi^+ \Delta S_n^+ \rho_n V}{A\Delta t} = -\frac{\phi^+ \Delta S_n^+ \rho_n Z}{\Delta t} \tag{55}$$

where Z is the thickness of the non-wetting mass accumulating before the interface (in case of fluid flow from a high to a low permeability domain) or the thickness of the suction zone (in case of fluid flow from a low to a high permeability domain). This parameter depends on the physics of the problem, mainly on the contrast between the entry pressures of the neighbouring layers, permeability of the involved materials and the applied fluid flux. Formulating an exact constitutive relationship for Z is beyond the scope of this work. Alternatively, we employed an iterative scheme for its determination such that the conservation of mass between the two sides of the boundary between two layers is maintained. The algorithm of this iterative scheme is:

0. **Do loop** over *i* (time steps)
1. $(S_n^i)^+ \leftarrow (S_n^{i+1})^+$
2. **Do loop** over *Z*
3. Initialize *Z*
4. Calculate ΔS_n^+, Eq. (54)
5. Calculate $q_n^{\Gamma d+}$, Eq. (55)
6. **Do loop** over *r* (nonlinear iterations)
7. Compute state vector increments, Eq. (41)
8. **End Do loop** over *r*.
9. If the conditions in Eqs. (42) and (43), for immobile and mobile non-wetting phase, are not satisfied, modify *Z* and go back to step 4. Otherwise exit the loop.
10. **End Do loop** over *Z*.
11. Calculate $(S_n^{i+1})^+$
12. **End Do loop** over *i*.

4 Verification and Numerical Examples

In this section, a verification example comparing the PUM-SG computational result to that obtained from a semi-analytical solution is studied. Additionally, two numerical examples

evaluating the numerical capabilities of the model for simulating layered medium domains exhibiting leakages are presented.

4.1 Model Verification

Van Duijn and De Neef [20] provided a semi-analytical solution based on the similarity solution technique to solve fluid flow in a two-layer system. The geometry constitutes two semi-infinite porous medium domains in-contact, as shown in Fig. 4. The left-hand side domain is initially saturated with a wetting phase, and the right-hand side domain is initially saturated with a non-wetting phase. With time, due to the capillary pressure, the wetting phase starts to infiltrate into the non-wetting phase domain. As expected, a jump in the saturation field occurs at the boundary between the two layers.

Fig. 4 Van Duijn and De Neef [20] domain and initial condition.

We solve this problem using the proposed PUM-SG model. The computational domain and boundary conditions are shown in Fig. 5. To compare to the semi-analytical solution, the following dimensionless parameters are utilized:

$$x^* = \frac{1}{L}x \; ; \; t^* = \frac{\sigma\sqrt{k^*}}{\mu_w L^2}t \; ; \; h^* = \left(\frac{k}{k^*\phi}\right)^{\frac{1}{2}} \; ; \; M = \frac{\mu_n}{\mu_w} \; ; \; F = \frac{\phi_r}{\phi_l} \tag{56}$$

in which x^* is a dimensionless distance from the interface, L is a reference quantity for length, x is the distance from the interface, t^* is a dimensionless time, σ is the interfacial tension, k^* is a reference permeability. We implemented $h_l^* = 1$, $h_r^* = 0.5$, $M = 1$, $F = 1$, pore size distribution index ($\hat{\theta}$) = 2, entry pressure at the left-hand side domain = $\sigma\sqrt{\phi_l / k_l}$, and entry pressure at the right-hand side = $\sigma\sqrt{\phi_r / k_r}$, as given by Van Duijn and De Neef [20].

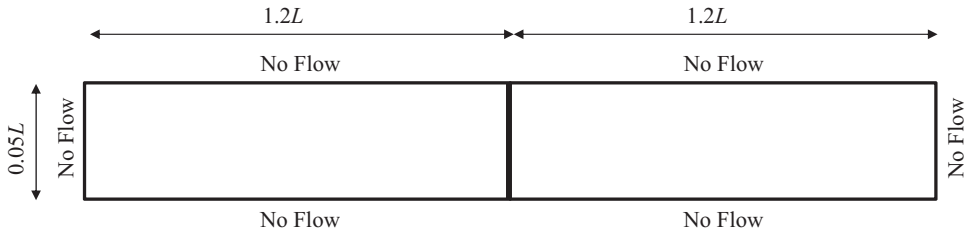

Fig. 5 Computational domain and boundary conditions.

Finite element meshes with different sizes are utilized: 75, 125 and 300 linear elements along the length of the domain (*x*-direction). Fig. 6 shows the computed results for the three mesh sizes, together with the semi-analytical solution of Van Duijn and De Neef [20]. The figure clearly shows that there is a good match between the two solutions, whereas the results obtained from the fine mesh is almost identical to the semi-analytical solution.

A convergence study is conducted to investigate the rate of convergence of the proposed model. The L_1 error norm is utilized, defined as

$$L_{1-\text{error}} = \int_{\Omega} \left| S_w - S_w^{ref} \right| d\Omega \tag{57}$$

where S_w^{ref} is the reference value calculated from the semi-analytical solution of Van Duijn and De Neef [20]. The error norms for three different points in time using four mesh sizes, 25, 75, 125, and 300 elements have been calculated. The results are plotted in Fig. 7 along with those reported by Friis and Evje [7], who solved the problem using the finite volume method with two different permeability averaging techniques: harmonic averaging and arithmetic averaging. The figure shows that the convergence rate of the proposed model is relatively high, several times higher than that based on the finite volume method.

Table 1 shows the error in jump in saturation versus mesh sizes for three points in time. The table clearly exhibits that with finer meshes, the error becomes smaller. Nevertheless, all mesh sizes give a reasonable error, which suggests that the method is mesh-independent.

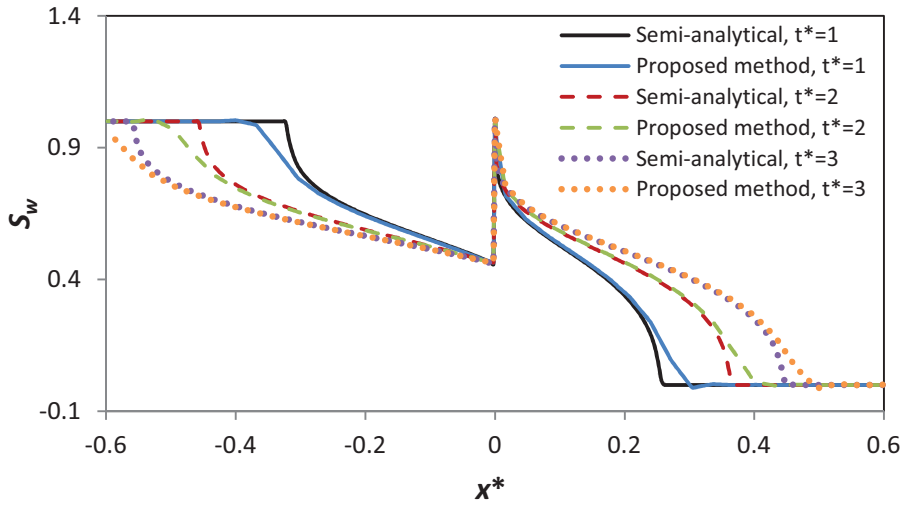

(a)

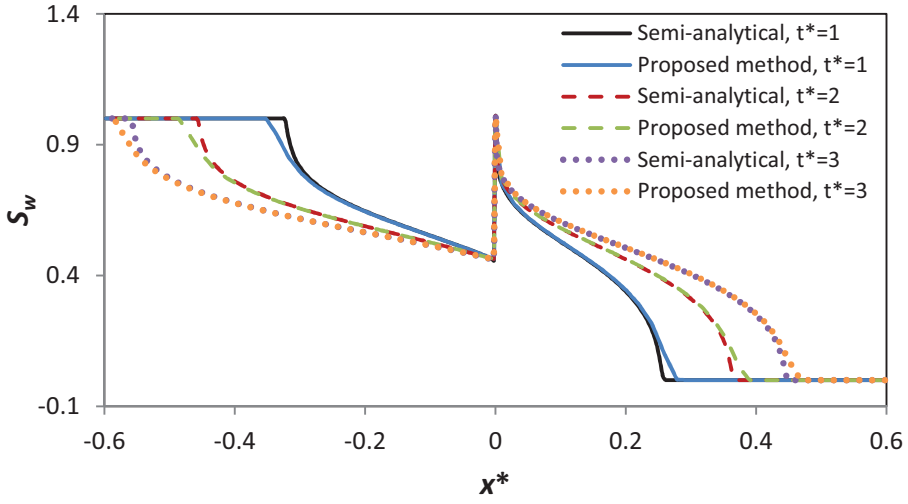

(b)

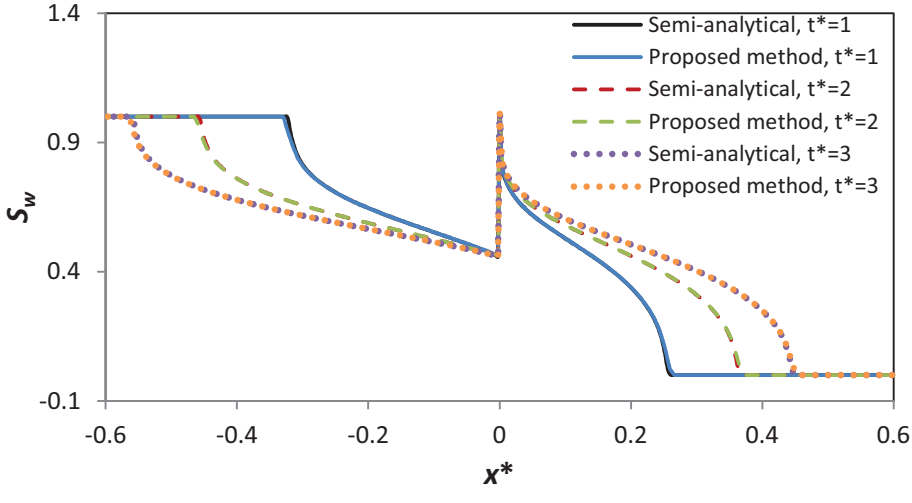

(c)

Fig. 6 PUM-SG versus Van Duijn and De Neef semi-analytical solution using: (a) 75 elements, (b) 125 elements, and (c) 300 elements.

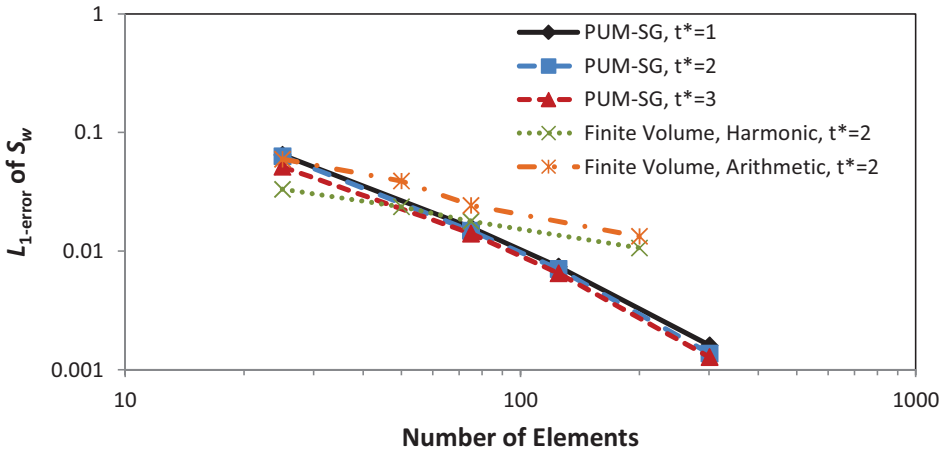

Fig. 7 Model convergence rate.

Table 1

Error in saturation discontinuity at three points in time.

Number of elements	Error (%)		
	t^*=1	t^*=2	t^*=3
25	0.74	3.74	3.62
75	3.69	0.88	0.24
125	1.44	0.15	0.99
300	1.12	0.15	0.18

4.2 DNAPL Infiltration

Helmig and Huber [2] and Fučík and Mikyška [4], among others, numerically examined the infiltration of a Dense Non-Aqueous Phase Liquid (DNAPL) in a multilayer system. The geometry constitutes a three-layer soil column, with a relatively high permeability (k_1) at the upper and lower layers, and a relatively low permeability (k_2) in the middle layer. The geometry of this problem together with the dimensions and boundary conditions are shown in Fig. 8.

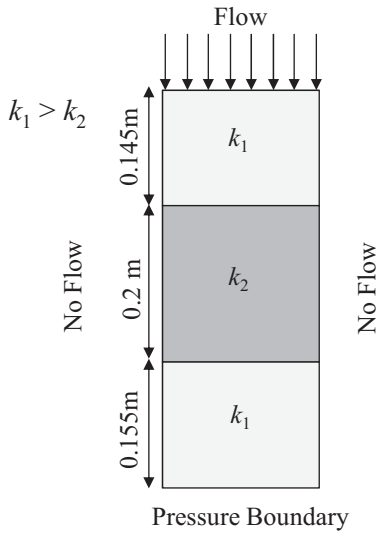

Fig. 8 DNAPL infiltration problem.

Initially, the domain is saturated with water. Then, DNAPL was injected from the upper boundary at a constant flow rate of 0.05 kg/s. The left- and right-hand side boundaries are closed to the flow, and a pressure boundary condition is defined at the lower boundary so that the water and DNAPL can freely exit the domain. The gravitational force is taken into account, and the Brooks-Corey relationships are utilized. Table 2 lists the fluid and layers properties, and Fig. 9 shows the corresponding Brooks and Corey diagrams.

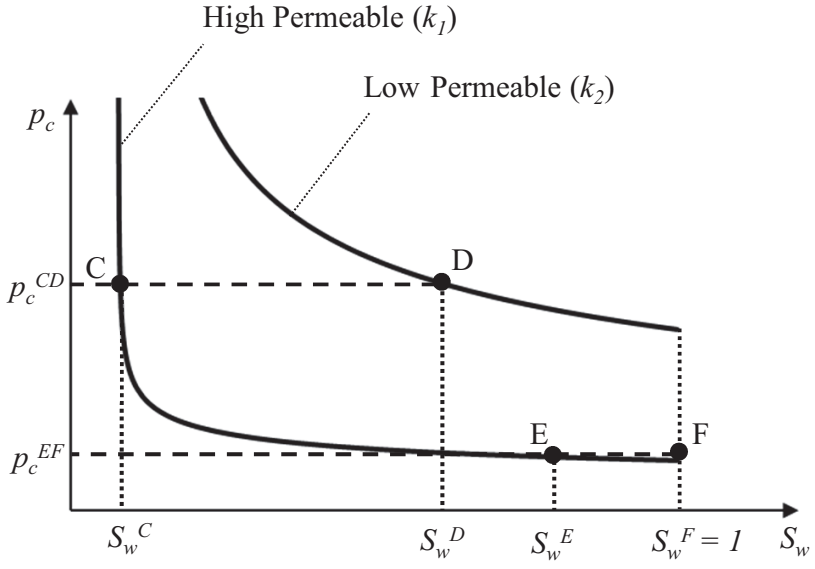

Fig. 9 Brooks and Corey diagrams for DNAPL infiltration example.

Table 2

Fluid and porous media properties for DNAPL infiltration problem.

Fluid properties	**Water**	**DNAPL**
Density [kg/m^3]	1000	1400
Viscosity [Pa.s]	0.001	0.001
Porous media properties	**Porous Medium #1 (high permeable)**	**Porous Medium #2 (low permeable)**
Permeability [m^2]	5.04×10^{-10}	5.26×10^{-11}
Porosity	0.4	0.39
Entry pressure (Brooks-Corey) [Pa]	370	1324
$\hat{\theta}$ (Brooks-Corey)	3.86	2.49
Water residual saturation	0.08	0.10
DNAPL residual saturation	0.00	0.00

We first utilized the standard Galerkin finite element method to solve the problem. Fig. 10 shows a DNAPL saturation distribution at time t = 1700 s using a relatively fine mesh (500 linear elements). It shows that there is a rise in the DNAPL saturation starting just before the boundary between the upper and middle layers and continuing in the middle layer. This behaviour is physically not correct as there should be an accumulation of DNAPL at the boundary between the two layers, followed by a jump in the saturation field. This erroneous result is expected since the standard Galerkin method is not capable of modelling the jump in the saturation field between layers of different hydraulic parameters. Helmig and Huber [2] have shown similar results for the standard Galerkin finite element method.

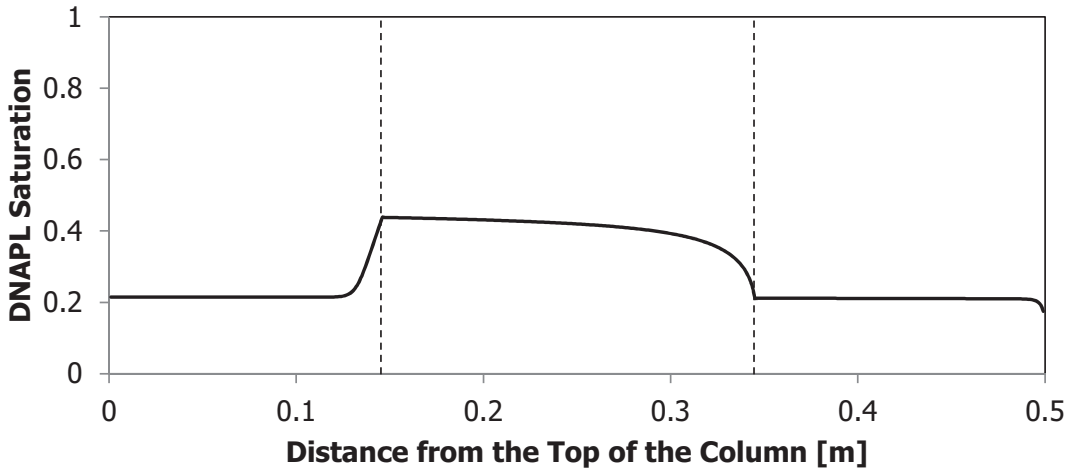

Fig. 10 Solution of DNAPL infiltration problem using standard Galerkin FEM method.

Fig. 11 shows the DNAPL saturation distribution at time t = 1700 s using the proposed PUM-SG model. Three finite element mesh sizes consisting of 25, 50 and 200 linear elements were utilized. The computational results show that the proposed model could capture accurately the saturation jump at the interfaces, even with the use of the relatively coarse mesh. However, the 25 elements mesh exhibits some errors before the jump, which is expected for such a coarse mesh. The 50 and 200 elements meshes exhibit accurate results in the whole domain. The computational results with 200 elements have been compared to the results given by Fučík and Mikyška [4], as illustrated in Fig. 12. It can be seen that the results are very close, though the PUM-SG results are more accurate at the suction interface, where it predicts full suction, while Fučík and Mikyška's model does not. The difference at the front location, however, is due to that Fučík and Mikyška have stopped their analysis at 1650 s, and we have stopped at 1700 s.

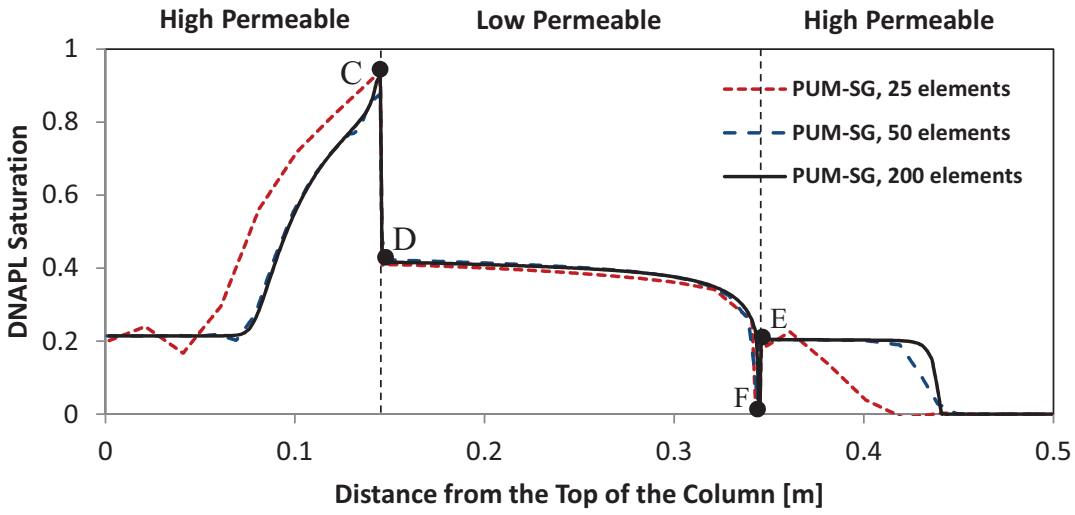

Fig. 11 Solution of DNAPL infiltration problem using PUM-SG model.

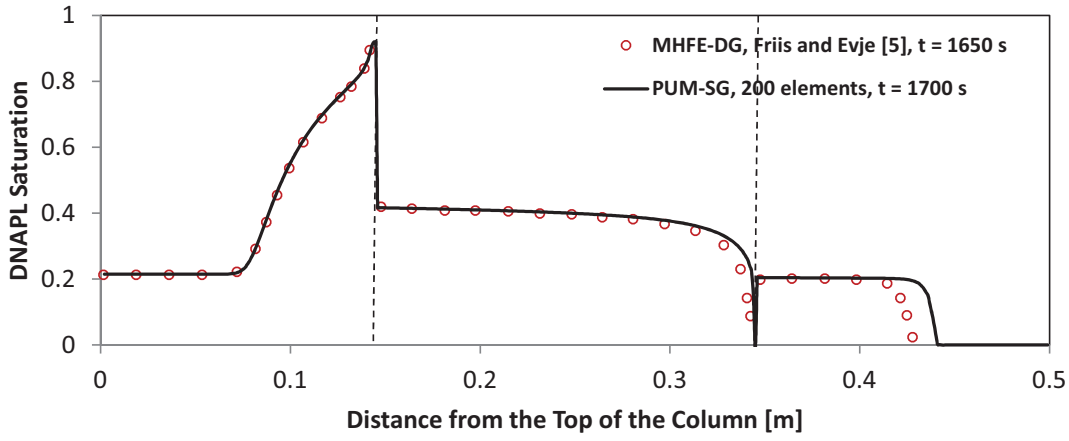

Fig. 12 PUM-SG versus Fučík and Mikyška model.

At the beginning, DNAPL accumulates at the boundary between the upper layer and the middle layer, on the upper layer side. In this case, the capillary pressure is discontinuous at the boundary. As the capillary pressure exceeds the entry pressure of the middle layer, DNAPL infiltrates into the middle layer. In this case, the capillary pressure is continuous and the saturation is discontinuous, as shown on points C and D on the Brooks and Corey diagram, Fig. 9.

On the boundary between the middle layer and the lower layer, suction occurs, appearing as a drop in the saturation profile before the boundary between the two layers and a sudden rise after the boundary. In this case, the entry pressure of the middle layer is initially higher than that of the lower layer, giving rise, upon the arrival of the DNAPL, to an immediate leakage. This behaviour corresponds to points E and F on the Brooks and Corey diagram in Fig. 9. Note that point F in Fig. 11 indicates $S_{\mathrm{DNAPL}} = S_n = 0$, which corresponds to $S_w = 1$ in Fig. 9.

4.3 CO_2 Leakage

CO_2 geo-sequestration is currently utilized as a means to mitigate CO_2 emission to the atmosphere in an attempt to reduce the likely greenhouse effect. Selection of an appropriate geological formation for CO_2 sequestration requires a good estimate of the amount of leakage that might take place in time. Leakage of CO_2 to the ground surface or upper layers containing ground water is considered as one of the main concerns of applying this technology.

This example demonstrates the computational capability and efficiency of the proposed model to simulate the likely leakage of CO_2 in a two-dimensional non-horizontally layered domain. The geometry is assumed to describe an aquifer bounded by a cap-rock and subjected to CO_2 injection. Fig. 13 shows the geometry and boundary conditions, and Table 3 lists the material and physical properties of the domain. The fluid and the porous medium properties of the aquifer are taken from the well-known benchmark leakage problem, which is utilized in literature to compare between numerical simulators [21]. For the cap-rock layer, the entry pressure is made 1.156 times that of the aquifer, and the permeability is made 0.375 times that of the aquifer. The Brooks and Corey relationships are assumed. The CO_2 is injected at a constant flow rate of 12.5 kg/day from the lower left corner of the aquifer. The gravity is taken into consideration so that the buoyancy forces will lead the CO_2 to flow upwards, towards the cap-rock. Because leakage is the main interest here, this set of material properties

and boundary conditions is imposed such that we observe a significant contrast in performance between the proposed model and models based on standard numerical schemes.

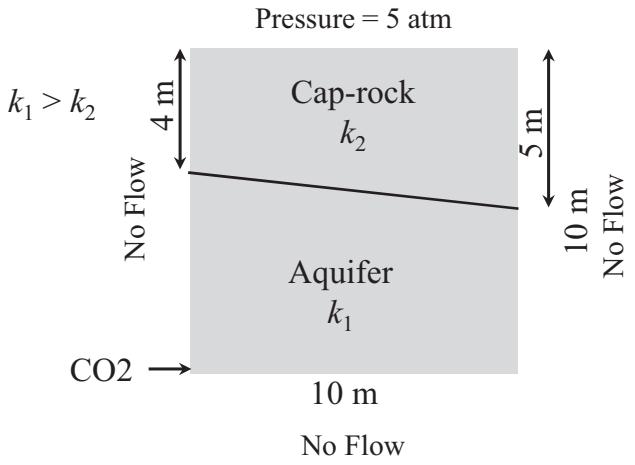

Fig. 13 Geometry and boundary conditions for the CO_2 injection problem.

This problem is solved using the standard Galerkin finite element method and the proposed PUM-SG model by means of five mesh sizes: 9, 25, 121, 225 and 400 linear elements. The finite element mesh for the SG must coincide with the boundary between the two layers, while for PUM-SG, this is not necessary. A structured mesh can be used for the PUM-SG model which enables the use of a standard simple mesh generator. Fig. 14 shows an example of these meshes.

Table 3

Fluid and domain properties for the problem of CO_2 injection.

Fluid properties	**Water**	**CO_2**
Density [kg/m^3]	1045	479
Viscosity [Pa.s]	2.535×10^{-4}	3.950×10^{-5}
Porous media properties	**Aquifer (high permeable)**	**Cap-rock (low permeable)**
Permeability [m^2]	2.0×10^{-14}	7.5×10^{-15}
Porosity	0.15	0.1
Entry pressure (Brooks-Corey) [kPa]	225	260
$\hat{\theta}$ (Brooks-Corey)	4.0	2.0
Water residual saturation	0.20	0.20
CO_2 residual saturation	0.00	0.00

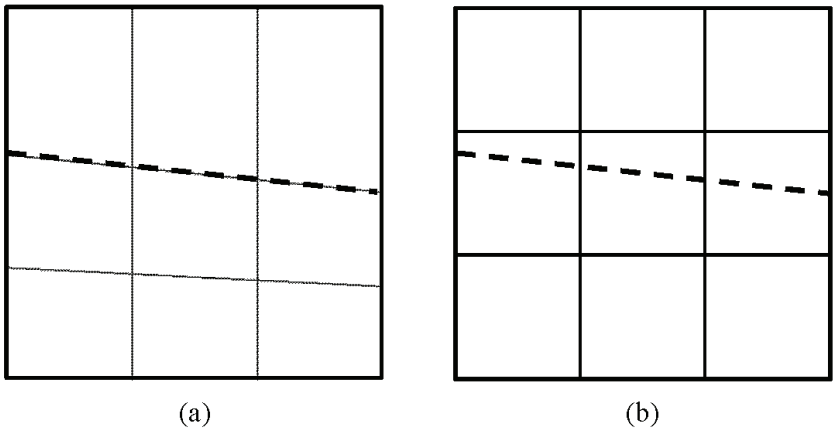

Fig. 14 Finite element meshes: (a) standard Galerkin model, and (b) PUM-SG model.

Fig. 15 shows the computational results of both models at time t = 82 days. Apparently, the standard Galerkin model, even for the relatively fine meshes, was not able to capture the jump in the saturation field at the boundary between the two layers, giving a false impression about the amount of leakage.

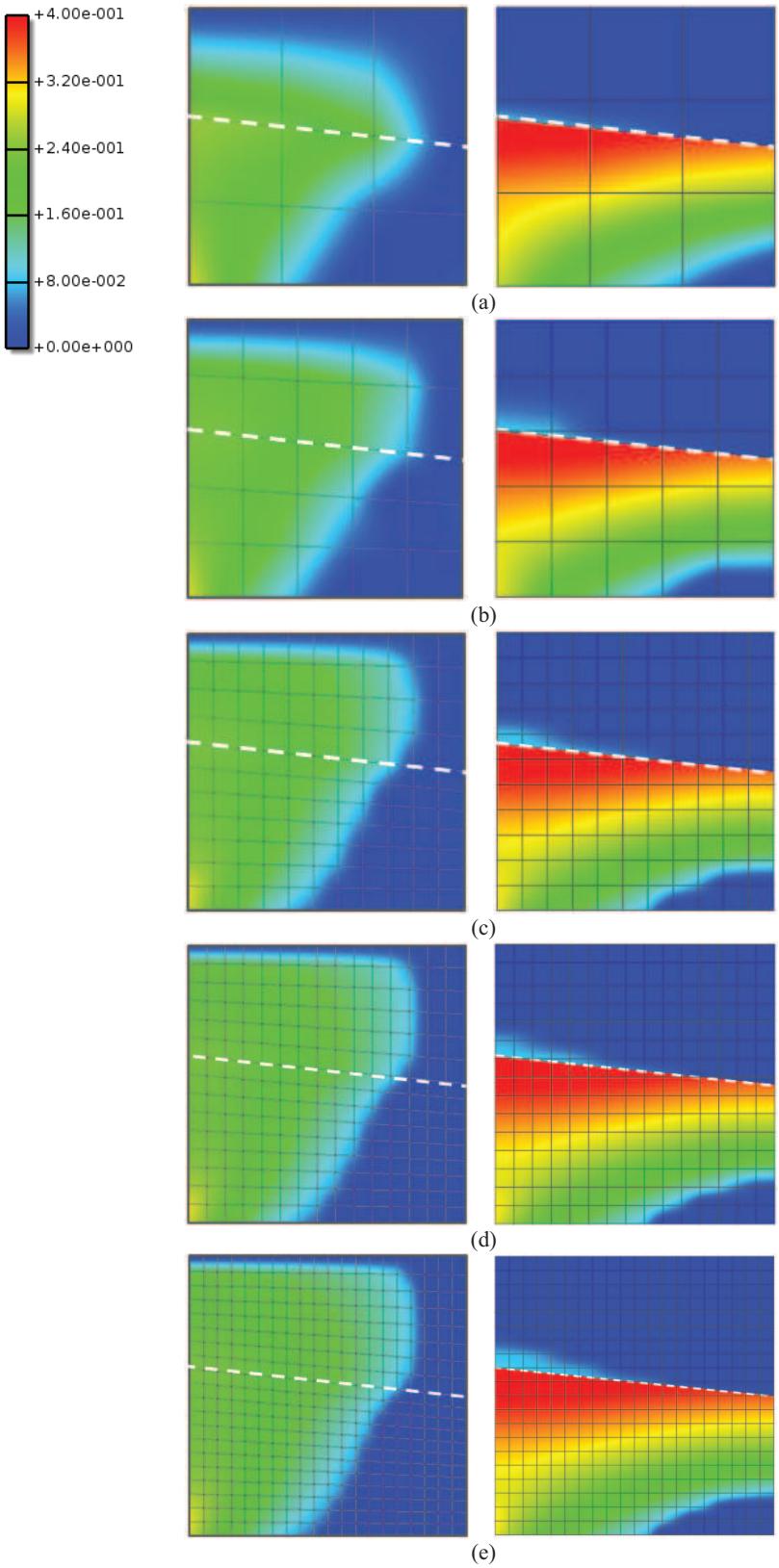

Fig. 15 CO_2 phase saturation distribution at t = 82 days. Left: standard Galerkin model; Right: PUM-SG model: (a) 9 elements, (b) 25 elements, (c) 121 elements, (d) 225 elements, (e) 400 elements.

On the other hand, the PUM-SG model could capture this phenomenon even with 9 elements, though the leakage was not as accurate. For 121 to 400 elements meshes, the computational results exhibit analogous accumulation and leakage, indicating that the model is effectively mesh-independent.

Fig. 16 shows the resulting pore pressure ($p = S_w p_w + S_n p_n$) obtained from the SG model and the PUM-SG model. Clearly, the figure shows a significant difference in the pore pressure distribution in the aquifer and the cap-rock layer between the two models. Failure to capture gas accumulation at the boundary between the aquifer and the cap-rock by the SG model leads to incorrect pore pressure distribution, and hence incorrect prediction of the mechanical behaviour of the CO_2 sequestration region.

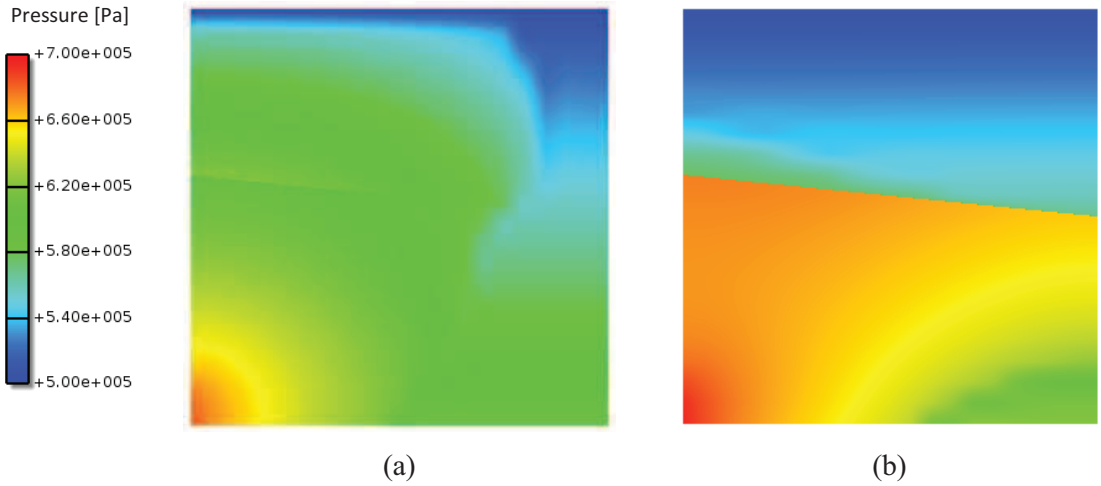

Fig. 16 Pore pressure distribution for the CO_2 leakage problem at t = 82 days (by using 400 elements): (a) SG model, and (b) PUM-SG model.

5 Conclusions

Leakage of fluids into underground formations is in many cases unwanted. Among others, contaminants, DNAPL and CO_2 leakage to the groundwater layers or to the ground surface is considered as one of the main concerns of applying geoenvironmental engineering technologies. This necessitates the development of computational tools capable of simulating this phenomenon accurately and efficiently.

In this work, we introduced a computationally efficient model capable of capturing a non-wetting phase leakage at the boundary between heterogeneous layers. A mixed discretization scheme is utilized. This scheme entails solving coupled balance equations using different

discretization schemes, which are tailored to accurately describe the physics of the primary state variables. We utilized the standard Galerkin finite element method to discretize the continuous water pressure field, and the partition of unity finite element method to discretize the discontinuous saturation field. The finite element formulation is three-dimensional (3D) but the computer implementation is two-dimensional (2D). The focus here is on the computational scheme which requires an intensive verification and validation study, that necessitates relatively short CPU time and small computer capacity. However, extension to 3D can be made using the usual finite element implementation practice.

The advantages of the proposed model is, in addition to its accuracy and robustness, its ability to embed the boundary between layers within the elements, allowing for the use of structured and geometry-independent meshes.

Acknowledgements

The authors acknowledge the financial support by Agentschap NL (Dutch Ministry of Economic Affairs) under grant number EOSLT07040.

Appendix A. Components of the finite element matrices

$$\mathbf{K}_{11} = \int_{\Omega} \nabla \mathbf{N}^T \mathbf{k} \lambda_w^r \nabla \mathbf{N} \, d\Omega \tag{A1}$$

$$\mathbf{K}_{12} = \int_{\Omega} \nabla \mathbf{N}^T \mathbf{k} \nabla \mathbf{N} \mathbf{p}_w^r \left(\frac{d\lambda_w}{dS_n} \mathbf{N} \right) d\Omega - \int_{\Omega} \nabla \mathbf{N}^T \mathbf{k} \rho_w \mathbf{g} \left(\frac{d\lambda_w}{dS_n} \mathbf{N} \right) d\Omega \tag{A2}$$

$$\mathbf{K}_{13} = \int_{\Omega} \nabla \mathbf{N}^T \mathbf{k} \nabla \mathbf{N} \mathbf{p}_w^r \left(\frac{d\lambda_w}{dS_n} \mathbf{N}^{eh} \right) d\Omega - \int_{\Omega} \nabla \mathbf{N}^T \mathbf{k} \rho_w \mathbf{g} \left(\frac{d\lambda_w}{dS_n} \mathbf{N}^{eh} \right) d\Omega \tag{A3}$$

$$\mathbf{K}_{21} = \int_{\Omega} \nabla \mathbf{N}^T \mathbf{k} \lambda_n^r \nabla \mathbf{N} \, d\Omega \tag{A4}$$

$$\begin{aligned} \mathbf{K}_{22} = & \int_{\Omega} \nabla \mathbf{N}^T \mathbf{k} \nabla \mathbf{N} \mathbf{p}_w^r \left(\frac{d\lambda_n}{dS_n} \mathbf{N} \right) d\Omega + \int_{\Omega} \nabla \mathbf{N}^T \mathbf{k} \eta_n^r \nabla \mathbf{N} \; d\Omega \\ & + \int_{\Omega} \nabla \mathbf{N}^T \mathbf{k} \nabla \mathbf{N} \mathbf{S}_n^r \left(\frac{d\eta_n}{dS_n} \mathbf{N} \right) d\Omega + \int_{\Omega^+} \nabla \mathbf{N}^T \mathbf{k} \nabla \mathbf{N}^{eh} \tilde{\mathbf{S}}_n^r \left(\frac{d\eta_n}{dS_n} \mathbf{N} \right) d\Omega \\ & - \int_{\Omega} \nabla \mathbf{N}^T \mathbf{k} \rho_n \mathbf{g} \left(\frac{d\lambda_n}{dS_n} \mathbf{N} \right) d\Omega \end{aligned} \tag{A5}$$

$$\mathbf{K}_{23} = \int_{\Omega} \nabla \mathbf{N}^T \mathbf{k} \nabla \mathbf{N} \mathbf{p}_w^r \left(\frac{d\lambda_n}{dS_n} \mathbf{N}^{eh} \right) d\Omega + \int_{\Omega^+} \nabla \mathbf{N}^T \mathbf{k} \eta_n^r \nabla \mathbf{N}^{eh} \, d\Omega$$
$$+ \int_{\Omega+} \nabla \mathbf{N}^T \mathbf{k} \nabla \mathbf{N}^{eh} \tilde{\mathbf{S}}_n^r \left(\frac{d\eta_n}{dS_n} \mathbf{N}^{eh} \right) d\Omega + \int_{\Omega} \nabla \mathbf{N}^T \mathbf{k} \nabla \mathbf{N} \mathbf{S}_n^r \left(\frac{d\eta_n}{dS_n} \mathbf{N}^{eh} \right) d\Omega \tag{A6}$$
$$- \int_{\Omega} \nabla \mathbf{N}^T \mathbf{k} \rho_n \mathbf{g} \left(\frac{d\lambda_n}{dS_n} \mathbf{N}^{eh} \right) d\Omega$$

$$\mathbf{K}_{31} = \int_{\Omega^+} \left(\nabla \mathbf{N}^{eh} \right)^T \mathbf{k} \lambda_n^r \nabla \mathbf{N} \, d\Omega \tag{A7}$$

$$\mathbf{K}_{32} = \int_{\Omega^+} \left(\nabla \mathbf{N}^{eh} \right)^T \mathbf{k} \nabla \mathbf{N} \mathbf{p}_w^r \left(\frac{d\lambda_n}{dS_n} \mathbf{N} \right) d\Omega + \int_{\Omega^+} \left(\nabla \mathbf{N}^{eh} \right)^T \mathbf{k} \eta_n^r \nabla \mathbf{N} \, d\Omega$$
$$+ \int_{\Omega^+} \left(\nabla \mathbf{N}^{eh} \right)^T \mathbf{k} \nabla \mathbf{N} \mathbf{S}_n^r \left(\frac{d\eta_n}{dS_n} \mathbf{N} \right) d\Omega + \int_{\Omega^+} \left(\nabla \mathbf{N}^{eh} \right)^T \mathbf{k} \nabla \mathbf{N}^{eh} \tilde{\mathbf{S}}_n^r \left(\frac{d\eta_n}{dS_n} \mathbf{N} \right) d\Omega \tag{A8}$$
$$- \int_{\Omega^+} \left(\nabla \mathbf{N}^{eh} \right)^T \mathbf{k} \rho_n \mathbf{g} \left(\frac{d\lambda_n}{dS_n} \mathbf{N} \right) d\Omega$$

$$\mathbf{K}_{33} = \int_{\Omega^+} \left(\nabla \mathbf{N}^{eh} \right)^T \mathbf{k} \nabla \mathbf{N} \mathbf{p}_w^r \left(\frac{d\lambda_n}{dS_n} \mathbf{N}^{eh} \right) d\Omega + \int_{\Omega^+} \left(\nabla \mathbf{N}^{eh} \right)^T \mathbf{k} \nabla \mathbf{N} \mathbf{S}_n^r \left(\frac{d\eta_n}{dS_n} \mathbf{N}^{eh} \right) d\Omega$$
$$+ \int_{\Omega^+} \left(\nabla \mathbf{N}^{eh} \right)^T \mathbf{k} \eta_n^r \nabla \mathbf{N}^{eh} \, d\Omega + \int_{\Omega^+} \left(\nabla \mathbf{N}^{eh} \right)^T \mathbf{k} \nabla \mathbf{N}^{eh} \tilde{\mathbf{S}}_n^r \left(\frac{d\eta_n}{dS_n} \mathbf{N}^{eh} \right) d\Omega \tag{A9}$$
$$- \int_{\Omega^+} \left(\nabla \mathbf{N}^{eh} \right)^T \mathbf{k} \rho_n \mathbf{g} \left(\frac{d\lambda_n}{dS_n} \mathbf{N}^{eh} \right) d\Omega$$

$$\mathbf{C}_{12} = - \int_{\Omega} \mathbf{N}^T \phi \mathbf{N} \, \delta d\Omega \tag{A10}$$

$$\mathbf{C}_{13} = - \int_{\Omega} \mathbf{N}^T \phi \mathbf{N}^{eh} d\Omega \tag{A11}$$

$$\mathbf{C}_{22} = \int_{\Omega} \mathbf{N}^T \phi \mathbf{N} \, d\Omega \tag{A12}$$

$$\mathbf{C}_{23} = \int_{\Omega} \mathbf{N}^T \phi \mathbf{N}^{eh} d\Omega \tag{A13}$$

$$\mathbf{C}_{32} = \int_{\Omega^+} \left(\mathbf{N}^{eh} \right)^T \phi \mathbf{N} \, d\Omega \tag{A14}$$

$$\mathbf{C}_{33} = \int_{\Omega^+} \left(\mathbf{N}^{eh} \right)^T \phi \mathbf{N}^{eh} d\Omega \tag{A15}$$

$$\mathbf{K}_{11}^{0} = \int_{\Omega} \nabla \mathbf{N}^{T} \mathbf{k} \lambda_{w}^{r} \nabla \mathbf{N} \, d\Omega \tag{A16}$$

$$\mathbf{K}_{21}^{0} = \int_{\Omega} \nabla \mathbf{N}^{T} \mathbf{k} \lambda_{n}^{r} \nabla \mathbf{N} \, d\Omega \tag{A17}$$

$$\mathbf{K}_{22}^{0} = \int_{\Omega} \nabla \mathbf{N}^{T} \mathbf{k} \eta_{n}^{r} \nabla \mathbf{N} \; d\Omega \tag{A18}$$

$$\mathbf{K}_{23}^{0} = \int_{\Omega} \nabla \mathbf{N}^{T} \mathbf{k} \eta_{n}^{r} \nabla \mathbf{N}^{eh} \; d\Omega \tag{A19}$$

$$\mathbf{K}_{31}^{0} = \int_{\Omega^{+}} \left(\nabla \mathbf{N}^{eh} \right)^{T} \mathbf{k} \lambda_{n}^{r} \nabla \mathbf{N} \, d\Omega \tag{A20}$$

$$\mathbf{K}_{32}^{0} = \int_{\Omega^{+}} \left(\nabla \mathbf{N}^{eh} \right)^{T} \mathbf{k} \eta_{n}^{r} \nabla \mathbf{N} \; d\Omega \tag{A21}$$

$$\mathbf{K}_{33}^{0} = \int_{\Omega^{+}} \left(\nabla \mathbf{N}^{eh} \right)^{T} \mathbf{k} \eta_{n}^{r} \nabla \mathbf{N}^{eh} \, d\Omega \tag{A22}$$

$$\mathbf{C}_{12}^{0} = -\int_{\Omega} \mathbf{N}^{T} \phi \mathbf{N} \, d\Omega \tag{A23}$$

$$\mathbf{C}_{13}^{0} = -\int_{\Omega} \mathbf{N}^{T} \phi \mathbf{N}^{eh} d\Omega \tag{A24}$$

$$\mathbf{C}_{22}^{0} = \int_{\Omega} \mathbf{N}^{T} \phi \mathbf{N} \, d\Omega \tag{A25}$$

$$\mathbf{C}_{23}^{0} = \int_{\Omega} \mathbf{N}^{T} \phi \mathbf{N}^{eh} d\Omega \tag{A26}$$

$$\mathbf{C}_{32}^{0} = \int_{\Omega^{+}} \left(\mathbf{N}^{eh} \right)^{T} \phi \mathbf{N} d\Omega \tag{A27}$$

$$\mathbf{C}_{33}^{0} = \int_{\Omega^{+}} \left(\mathbf{N}^{eh} \right)^{T} \phi \mathbf{N}^{eh} d\Omega \tag{A28}$$

$$\mathbf{f}_{1} = \int_{\Omega} \nabla \mathbf{N}^{T} \mathbf{k} \lambda_{w}^{r} \rho_{w} \mathbf{g} d\Omega - \frac{1}{\rho_{w}} \int_{\Gamma_{w}^{q}} \mathbf{N}^{T} \hat{q}_{w} d\Gamma \tag{A29}$$

$$\mathbf{f}_{2} = \int_{\Omega} \nabla \mathbf{N}^{T} \mathbf{k} \lambda_{n}^{r} \rho_{n} \mathbf{g} d\Omega - \frac{1}{\rho_{n}} \int_{\Gamma_{n}^{q}} \mathbf{N}^{T} \hat{q}_{n} d\Gamma \tag{A30}$$

$$\mathbf{f}_{3} = \int_{\Omega^{+}} \left(\nabla \mathbf{N}^{eh} \right)^{T} \mathbf{k} \lambda_{n}^{r} \rho_{n} \mathbf{g} d\Omega - \frac{1}{\rho_{n}} \int_{\Gamma_{n}^{q+}} \left(\mathbf{N}^{eh} \right)^{T} \hat{q}_{n} d\Gamma + \frac{1}{\rho_{n}} \int_{\Gamma_{d}} \left(\mathbf{N}^{eh} \right)^{T} q_{n}^{\Gamma_{d}} \, d\Gamma \tag{A31}$$

References

[1] Van Duijn C, Molenaar J, De Neef M. The effect of capillary forces on immiscible two-phase flow in heterogeneous porous media. Transp Porous Media 1995;21:71-93.
[2] Helmig R, Huber R. Comparison of Galerkin-type discretization techniques for two-phase flow in heterogeneous porous media. Adv Water Resour 1998;21:697-711.
[3] Van Duijn C, Mikelic A, Pop IS. Effective equations for two-phase flow with trapping on the micro scale. SIAM J Appl Math 2002;62:1531-68.
[4] Fučík R, Mikyška J. Mixed-hybrid finite element method for modelling two-phase flow in porous media. J Math Ind 2011;3:9-19.
[5] Brooks RH, Corey AT. Hydraulic properties of porous media. Hydrology Paper No 3, Colorado State Univ, Fort Collins, Colorado 1964.
[6] van Genuchten MT. A closed-form equation for predicting the hydraulic conductivity of unsaturated soils. Soil Sci Soc Am J 1980;44:892-8.
[7] Friis HA, Evje S. Numerical treatment of two-phase flow in capillary heterogeneous porous media by finite-volume approximations. Int J Numer Anal Model 2011;9:505-28.
[8] Brenner K, Cancès C, Hilhorst D. Finite volume approximation for an immiscible two-phase flow in porous media with discontinuous capillary pressure. Comput Geosci 2013;17:573-97.
[9] Cances C. Finite volume scheme for two-phase flows in heterogeneous porous media involving capillary pressure discontinuities. ESAIM: Math Model Numer Anal 2009;43:973-1001.
[10] Szymkiewicz A, Helmig R, Kuhnke H. Two-phase flow in heterogeneous porous media with non-wetting phase trapping. Transp Porous Media 2011;86:27-47.
[11] Babuška I, Melenk JM. The Partition of Unity Method. Int J Numer Methods Eng 1997;40:727-58.
[12] Lewis RW, Schrefler BA. The finite element method in the static and dynamic deformation and consolidation of porous media. Chichester [u.a.]: Wiley; 2000.
[13] Al-Khoury R, Sluys LJ. A computational model for fracturing porous media. Int J Numer Methods Eng 2007;70:423-44.
[14] Talebian M, Al-Khoury R, Sluys LJ. Coupled electrokinetic–hydromechanic model for CO2 sequestration in porous media. Transp Porous Media 2013;98:287–321.
[15] Talebian M, Al-Khoury R, Sluys LJ. A computational model for coupled multiphysics processes of CO2 sequestration in fractured porous media. Adv Water Resour 2013;59:238-55.
[16] OPM (Open Porous Media) initiative, DuMux documentation. http://www.dumux.org/doxygen-trunk/html/class_dumux_1_1_regularized_brooks_corey.php (accessed June 16, 2014).
[17] Barrett J, Knabner P. Finite Element Approximation of the Transport of Reactive Solutes in Porous Media. Part 1: Error Estimates for Nonequilibrium Adsorption Processes. SIAM J Numer Anal 1997;34:201-27.
[18] Pop IS, Radu F, Knabner P. Mixed finite elements for the Richards' equation: linearization procedure. J Comput Appl Math 2004;168:365-73.
[19] Qin L, Peszynska M, Wheeler MF. A parallel multiblock black-oil model in multimodel implementation. SPE J 2002;7:278-87.
[20] Van Duijn CJ, De Neef MJ. Similarity solution for capillary redistribution of two phases in a porous medium with a single discontinuity. Adv Water Resour 1998;21:451-61.
[21] Class H, Ebigbo A, Helmig R, Dahle H, Nordbotten J, Celia M, et al. A benchmark study on problems related to CO2 storage in geologic formations. Comput Geosci 2009;13:409-34.